



Green synthesized AgNPs decorated on Ketjen black for enhanced catalytic dye degradation

Rajavaram Ramaraghavulu¹ · V. Koteswara Rao² · K. C. Devarayapalli³ · Kisoo Yoo³ · P. C. Nagajyothis³ · Jaesool Shim³

Received: 20 July 2020 / Accepted: 29 September 2020
© Springer Nature B.V. 2020

Abstract

The green synthesis of nanoparticles using plant-based materials as an alternative to chemical and physical routes provides economic and environmental benefits. In the present study, silver nanoparticles (AgNPs) were fabricated using *Pseudocycdonia sinensis* fruit extract. The fabricated NPs were then decorated on commercial Ketjen black-300 (AgNPs@KB-300) and Ketjen black-600 (AgNPs@KB-600). The synthesized materials were characterized via XRD, FTIR, XPS, SEM-EDX, and HR-TEM studies. The SEM and HR-TEM results revealed that the synthesized AgNPs were spherical and successfully decorated on KB-300 and KB-600. Additionally, the catalytic ability of the synthesized samples during the degradation of methyl orange in the presence of NaBH₄ was studied. Notably, the catalytic activity of AgNPs@KB-600 was higher than that of AgNPs@KB-300.

Keywords Green synthesis · AgNPs · Ketjen black · Methyl orange · Catalytic activity

Electronic supplementary material The online version of this article (<https://doi.org/10.1007/s11164-020-04290-w>) contains supplementary material, which is available to authorized users.

✉ P. C. Nagajyothis
nagajyothis@ynu.ac.kr

✉ Jaesool Shim
jshim@ynu.ac.kr

¹ Department of Humanities and Sciences, Annamacharya Institute of Technology and Sciences, Rajampet, Kadapa 516126, India

² Korea Center for Artificial Photosynthesis, Department of Chemistry, Sogang University, Seoul 04107, South Korea

³ School of Mechanical Engineering, Yeungnam University, Gyeongsan 38541, Republic of Korea

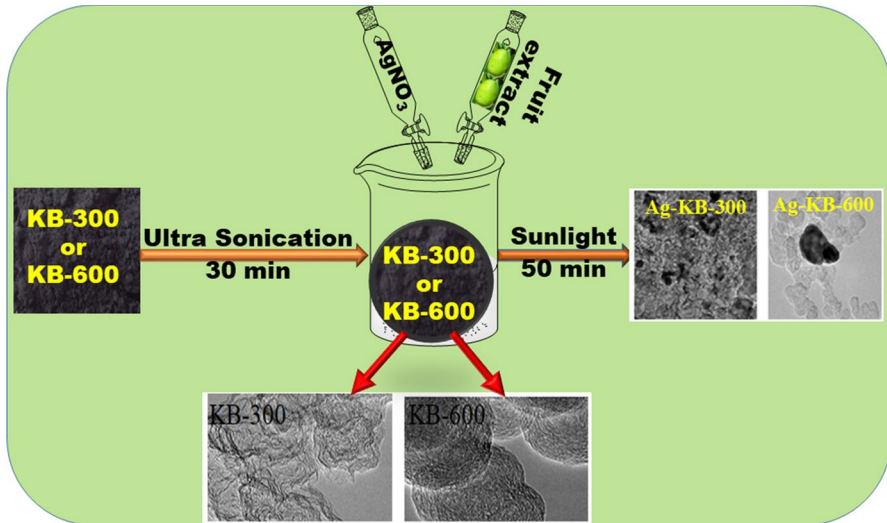
Introduction

Nowadays, it is becoming increasingly crucial to ensure that our environment is pollution-free. Point source pollution occurs mainly from municipal wastewater treatment plants and industrial effluents. The discharge of industrial effluents into water bodies has harmful effects on humans, animals, and aquatic life [1]. Methyl orange ($C_{14}H_{14}N_3NaO_3S$), is an anionic dye that is extensively used in dyeing, textile, printing, and pharmaceutical industries [2, 3]. When oral consumption, it is toxic as well as carcinogenic owing to the presence of nitrogen [4]. Various chemical, physical, and biological methods are used for the degradation of these dyes. However, the degradation of dyes using green synthesized NPs as a catalyst in the presence of $NaBH_4$ is an eco-friendly manner.

Among various metal NPs, silver nanoparticles (AgNPs) exhibit high catalytic activity owing to their size and large surface to volume ratio [5]. Several methods have been used to synthesize of AgNPs. These include chemical reduction [6], microwave synthesis [7], photochemical synthesis [8], reverse microemulsion polymerization [9], electrochemical [10], biological synthesis using bacteria and fungus [11, 12], and green synthesis [13, 14]. The green synthesis method is facile, rapid, and environmentally benign. In addition, green synthesized AgNPs decorated on carbon-based materials are widely used in various applications such as photocatalytic (AgNPs/g- C_3N_4 ; Ag decorated rGO) [15, 16], catalytic dye degradation (AgNPs/GO) [17], antibacterial (AgNPs/MWCNTs) [18], electrochemical sensing (AgNPs/rGO) [19], anticancer (AgNPs/rGO) [20], and cytotoxic (AgNPs/GO) [21], sensing of heavy metals (Ag@rGONCs) [22], and photocatalytic bacteria inactivation studies [13].

Carbon-based materials (GO, rGO, g- C_3N_4 , CNTs, QDs, carbon nanofibers, and Ketjen black) have outstanding physicochemical, thermal, optical properties, excellent electrical conductivity, corrosion resistance, and inexpensive. Such materials are generally used as supporters [23–29]. Among the carbon-based materials, Ketjen black (KB) is a conductive material with a large surface area, excellent conductivity, and good structural stability [23]. It is widely used as a supporter in lithium-sulfur batteries (CeO₂ nanodots decorated on Ketjen black) [30], lithium-ion batteries (γ -Fe₂O₃NP/Ketjen black) [31], glucose electrooxidation (Ketjen black as supports of Pt) [32], oxygen reduction reactions (nitrogen-doped Ketjen black-supported Co₃O₄ NPs; MnO_x-CeO₂/Ketjen black) [23, 33], hydrogen evolution (Mo₂C NPs embedded in Ketjen black) [34], and supercapacitor (Ketjen black supported polyanthraquinone) applications [35].

Pseudocystidia sinensis (Chinese quince; family Rosaceae) is native to East Asia; it is generally called ‘mugua’ in China, whereas in Korea it is called ‘mogwa’. Its dried fruits have been used in traditional Chinese medicine [36–38]. Green synthesis of metal NPs decorated on carbon materials and the application of such NPs in catalytic dye degradation has been limited. In this paper, we report the synthesis of AgNPs using *Pseudocystidia sinensis* dried fruit as a reducing agent. The synthesized NPs decorated on commercial Ketjen black 300 and 600 were labeled as AgNPs@KB-300 and AgNPs@KB-600, respectively (Scheme 1).



Scheme 1. Synthesis of AgNPs@KB-300 or 600

Furthermore, the synthesized samples were used as catalysts in the degradation of methyl orange (MO) in the presence of NaBH_4 . Compared to AgNPs@KB-300, AgNPs@KB-600 exhibited higher catalytic degradation.

Materials and methods

Synthesis of AgNPs@KB-300 and AgNPs@KB-600

First 50 mg of commercial Ketjen black 300 (KB-300) or Ketjen black 600 (KB-600) was ultrasonically dispersed into 450 mL of double-distilled water for approximately 60 min. Subsequently, the required quantity of AgNO_3 (1 mM) was added to the KB-300 or KB-600 solution and then stirred for 30 min at room temperature. Next, 50 mL aqueous extract of dried *Chinese quince* fruits was added and stirred 10 min and the solution was then kept under direct sunlight for 50 min, and a black turbid solution was formed. The reduction of metal (Ag^+) ions occurred immediately, and AgNPs@KB-300 and AgNPs@KB-600 formed within 50 min. Synthesized characterization was discussed in the supplementary information.

Catalytic activity

The MO dye was selected for this decolorization experiment. The MO decolorization experiment (2 mL; 10 ppm; Sigma-Aldrich) was performed in the presence of NaBH_4 (0.3 mL; 0.2 M; Sigma-Aldrich) and 35 μL aqueous solution of a

well-dispersed catalyst (2.5 mg/mL). The dye decolorization was monitored by UV–Visible spectroscopy (Neogen, NEO-D3117).

Results and discussion

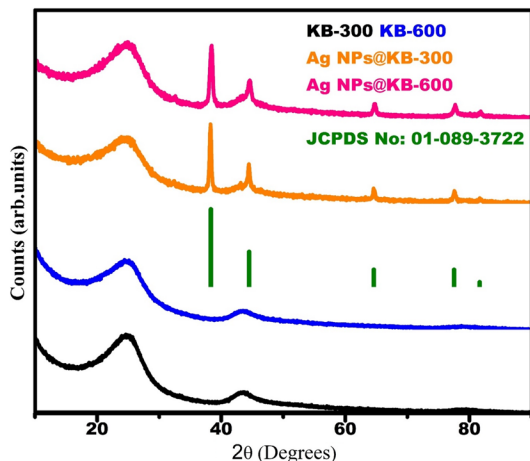
Characterization

XRD

Figure 1 shows the XRD pattern of pure KB-300, KB-600, AgNPs@KB-300, and AgNPs@KB-600 samples. Pure KB exhibited two diffraction peaks: one was a weak diffraction peak around 43.42° , corresponding to the (100) plane and the second one was a broad and strong peak located at 24.5° , corresponding to the (002) plane of the graphite carbon structure. Notably, the (002) peak was wider in the case of KB-600 than that in the case of KB-300. For the AgNPs@KB-300 and AgNPs@600 sample, the Ag diffraction peaks at $2\theta = 38.17^\circ$ and 38.41° ; 44.48° and 44.60° ; 64.68° and 64.80° ; 77.42° and 77.77° were attributed to the (111), (200), (220), and (311) planes, respectively. Furthermore, the size of the crystallite was calculated using Scherrer's formula. The calculated crystalline size was ~ 39.0 and ~ 19.0 nm for AgNPs@KB-300 and AgNPs@KB-600, respectively. In these samples, the Ag was pure and crystalline, with no other obvious phases present.

The peak broadening induced strain and the size were calculated from the Williamson-Hall (W-H) plot using the XRD profiles. The plots of $4 \sin \theta$ with respect to $\beta \cos \theta$ for AgNPs@KB300 and AgNPs@KB600 are shown in Fig. S1. The microstrain and crystallite sizes were estimated from the fitted linear curve. The crystallite size was calculated from the y -intercept using the relationship $y - \text{intercept} = \frac{K\lambda}{\text{Size}}$. Furthermore, the microstrain was calculated using the slope of the fitted curve using the relationship $\text{slope} = 4 \times \text{strain} \times \sin \theta$. In the present investigation, the crystallite size was estimated from the W-H plot as 30 and 28 nm for AgNPs@KB300

Fig. 1 XRD spectrum of green synthesized AgNPs decorated on KB-300 and KB-600



and AgNPs@KB600, respectively. Chen et al. [39] and Xie et al. [40] suggested that nano-crystallization also has an excellent degradation effect. The estimated microstrain for the AgNPs@KB600 and AgNPs@KB300 samples was 0.0052 and 0.00033, respectively. The slopes positively reflected the tensile strain present in the samples.

FT-IR

The functional groups of the AgNPs@KB-300 and AgNPs@KB-600 were determined via FT-IR spectroscopy. In KB-300 and 600, the peak close to 1600 cm^{-1} was attributed to the C=C stretching vibration, whereas the peaks at approximately 1050 cm^{-1} corresponded to the C–O stretching [41] (Fig. S2). The FT-IR spectra of AgNPs@KB-300 and AgNPs@KB-600 are shown in Fig. S3. Some prominent AgNPs@KB-300 and AgNPs@KB-600 peaks were observed at 2670 cm^{-1} and 2659 cm^{-1} ; 2349 cm^{-1} and 2364 cm^{-1} ; 1272 cm^{-1} and 1265 cm^{-1} ; and 846 cm^{-1} and 842 cm^{-1} , respectively. These were related to the C–H alkane stretching, O=C=O carbonyl bond group stretching, C–N stretching amines, and C=CH₂ groups, respectively [42–44]. After the green synthesized AgNPs were decorated onto KB-300 and 600, C=C, C–O functional groups were still present with slight changes.

Morphological studies

The SEM images revealed the spherical shape of the AgNPs attached to the surfaces of KB-300 and KB-600. For, both samples, most of the nanoparticles were spherical (Fig. 2ai–iii, bi–iii). The EDX and elemental mapping indicated the presence of Ag and C (2a iv–vi and b-iv–vi). Therefore, these results confirmed that the green synthesized AgNPs were successfully attached to KB-300 and KB-600.

Figure 3 shows the TEM images of the pristine KB-300 (Fig. S4 a and b), KB-600 (Fig. S4 c and d), AgNPs@KB-300, and AgNPs@KB-600 samples, respectively. Both pristine KB-300 and KB-600 showed a similar sheet-type and porous sphere-like morphology. In both AgNPs@KB-300 and AgNPs@KB-600 samples, the green synthesized AgNPs decorated were eventually (3a i–ii and bi–ii). Furthermore, the lattice fringes of 0.242 nm in spacing corresponded to the (111) plane of Ag (3 a-iii and b-iii). The corresponding line profiles are shown in Fig. S5 and Fig. S6 for AgNPs@KB-300 and AgNPs@KB-600, respectively. Hence, it is evident that AgNPs were decorated on the surfaces of KB-300 and KB-600.

XPS

XPS technique was carried out to identify and confirm the chemical state of AgNPs@KB-600. The XPS analysis was carried out only on one sample (AgNPs@KB-600), and the results are shown in Fig. 4. The survey scan spectra of AgNPs@KB-600 are shown in Fig. 4a, which reveals the presence of Ag and C with an additional peak of O. To obtain more information regarding the Ag and C metals, we performed high-resolution XPS analysis. Figure 4b shows the deconvoluted high-resolution XPS spectra of C, which contained three dominant peaks at

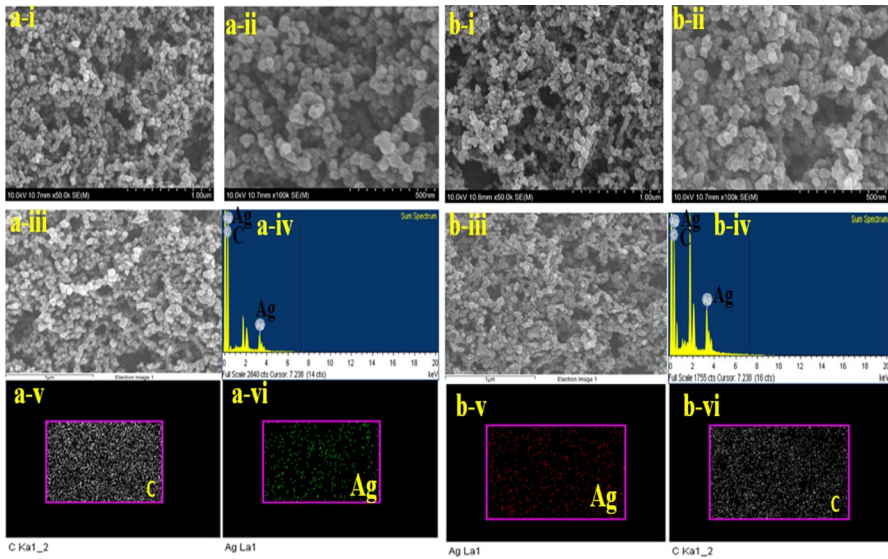


Fig. 2 SEM images of AgNPs@KB-300 (a-i–a-iii), AgNPs@KB-600 (b-i–b-iii), EDX spectra of AgNPs@KB-300 (a-iv), AgNPs@KB-600 (b-iv), and elemental mapping of AgNPs@KB-300 (a-v and b-v) and Ag@KB-600 (b-v and b-vi)

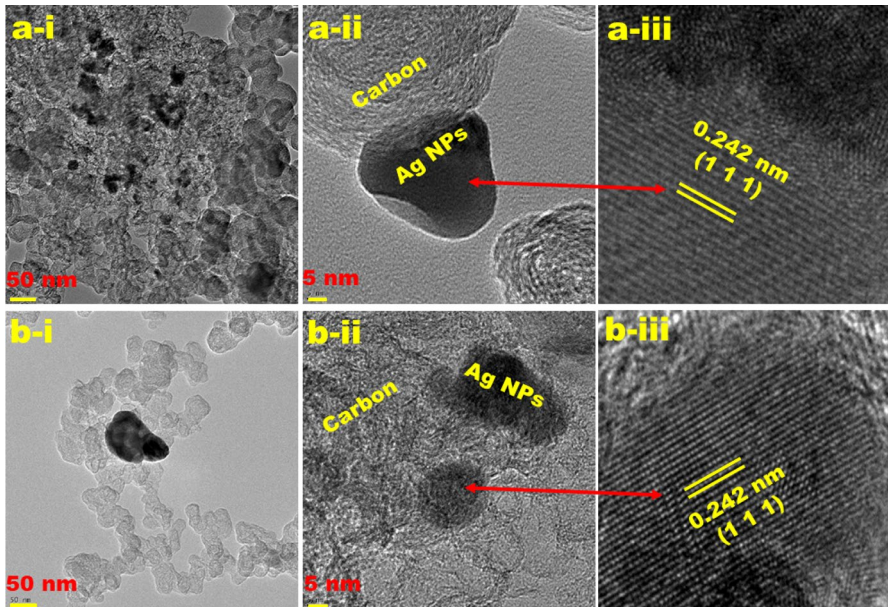


Fig. 3 Low-magnification TEM images of AgNPs@KB-300 (a-i), AgNPs@KB-600 (b-i), high magnification HR-TEM images of AgNPs@KB-300 (a-ii), AgNPs@KB-600 (b-ii), and d-spacing values of AgNPs@KB-300 (a-iii) and AgNPs@KB-600 (b-iii)

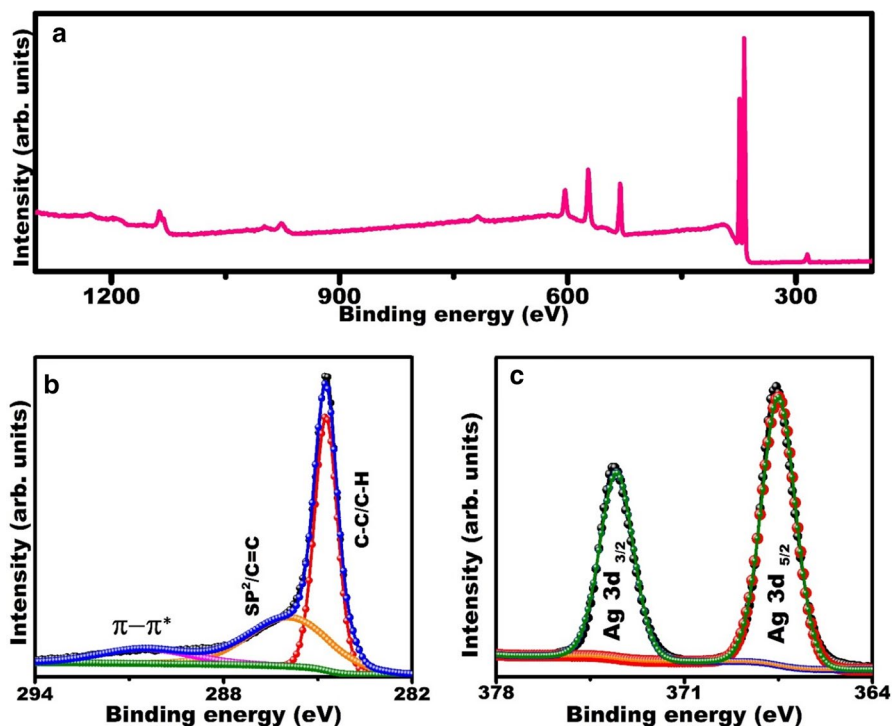


Fig. 4 XPS spectra of AgNPs@KB-600 (a); survey scan and high-resolution scans spectra of C 1s (b) and Ag 3d (c)

various binding energies. The peaks observed at binding energies of 284.7, 285.9, and 290.6 eV were attributed to C–C, C=C, and $\pi - \pi^*$ groups, respectively [45]. Figure 4c shows the high-resolution XPS spectra of Ag 3d. Particularly, the spectra exhibit doublet peaks which arose from the spin–orbit coupling Ag 3d_{3/2} and Ag 3d_{5/2}; the corresponding peaks are located at 373.5 and 367.5 eV, respectively. The splitting of the 3d doublet of Ag was approximately 6.0 eV, indicating that Ag was formed on the surface of Ketjen black [46].

Figure 5 shows the BET surface analysis of AgNPs@KB-300 and AgNPs@KB-600. The BET surface area was found to be 225.89 m² g⁻¹ with a pore volume of 0.578108 cm³ g⁻¹ for AgNPs@KB-300 and 288.97 m² g⁻¹ with a pore volume of 0.640988 cm³ g⁻¹ for AgNPs@KB-600. The AgNPs@KB-600 had the largest surface area (288.97 m² g⁻¹), which can affect the catalytic dye degradation activity.

Catalytic studies

Water pollution is mainly caused by industrial effluents, which contain various organic dye pollutants and toxic metals, these are harmful to organisms. Catalytic degradation is a suitable way to decompose toxic dyes. This method is

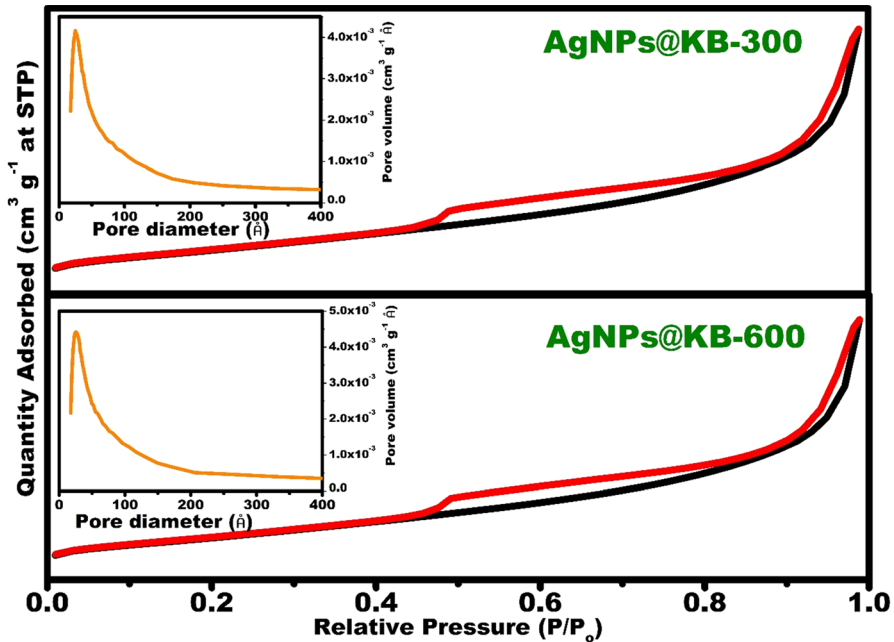


Fig. 5 BET surface area of green synthesized AgNPs, AgNPs@KB300 (above) and AgNPs@KB600 (below) nitrogen adsorption–desorption isotherms (inset: corresponding pore-size distribution)

simple, rapid, and inexpensive. In this study, MO was selected as a model pollutant to examine the catalytic activity of the KB-300, KB-600, AgNPs@KB-300, and AgNPs@KB-600 nanocatalysts, with sodium borohydride (NaBH_4) under ambient conditions. MO shows a strong absorption peak of ~ 464 nm owing to the absorption exhibited by the azo group. Furthermore, a weak absorption peak at 272 nm was ascribed to the $\pi - \pi^*$ transition in the aromatic rings [47]. Figure 6 shows the UV–visible spectrum of the catalytic activity compression of the synthesized samples. The KB-300 (Fig. 6a) and KB-600 (Fig. 6b) samples showed ~ 45 and $\sim 50\%$ degradation, respectively, within 14 min, in the presence of NaBH_4 . Moreover, the dye decolorization occurred rapidly in the presence of the AgNPs@KB-300 (Fig. 6c) and AgNPs@KB-600 (Fig. 6d), and NaBH_4 in the reaction solution (MO dye) owing to the increase of electron transfer from catalyst to the dye. The percentage of degradation of dye was calculated using the following equation:

$$\% \text{ degradation} = \frac{C_o - C}{C_o} \times 100 \quad (1)$$

where C_o is the initial concentration of dye before illumination and C is the concentration of the dye after time t . The Langmuir–Hinshelwood pseudo-first-order kinetic model equation was used to determine the rate constant according to the following equation [48]:

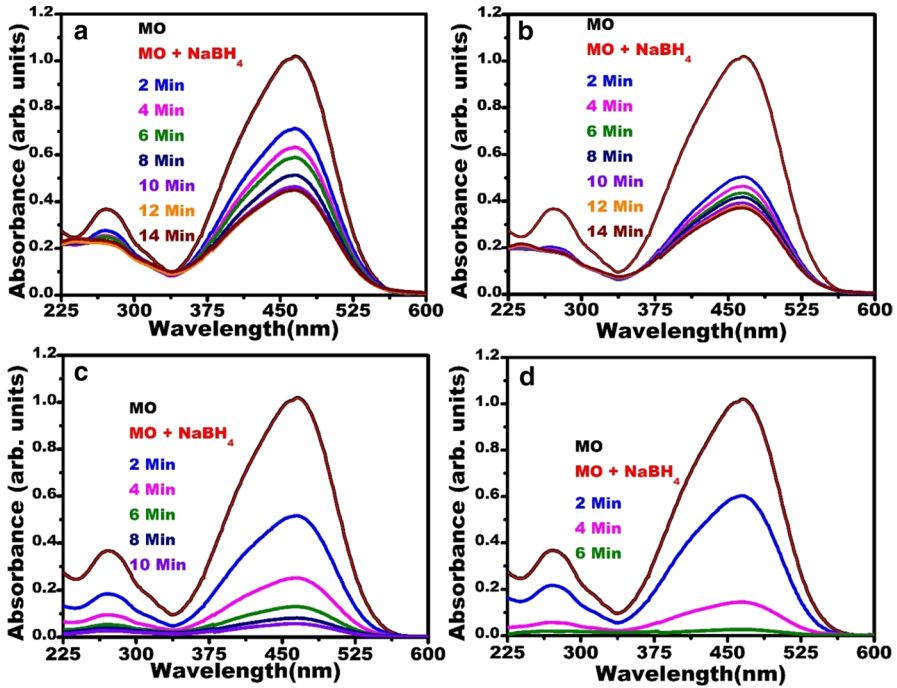


Fig. 6 Time-dependent of MO UV-Visible spectrum on NaBH_4 in the presence of KB-300 (a), KB-600 (b), AgNPs@KB-300 (c), and AgNPs@KB-600

$$\ln\left(\frac{C}{C_0}\right) = -kt \tag{2}$$

where k is the apparent first-order rate constant (min^{-1}), and t is the time interval. The MO dye decolorization performance of the green synthesized catalysts (KB-300, KB-600, AgNPs@KB-300, and AgNPs@KB-600) is shown in Fig. 7a. This figure reveals that AgNPs@KB-600 exhibited excellent MO dye decolorization

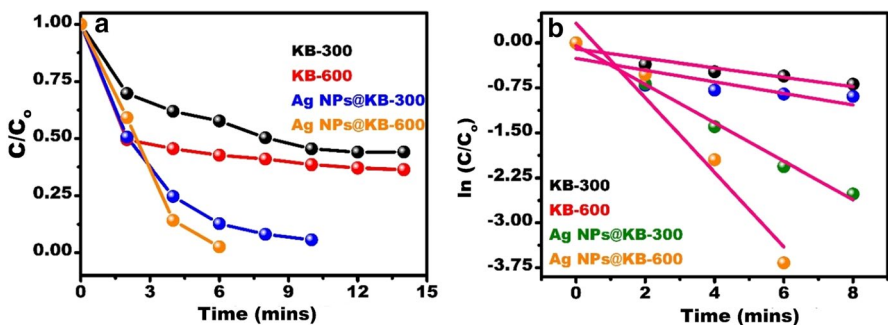


Fig. 7 MO dye degradation efficiency of green synthesized AgNPs on KB-300 and KB-600 (a) and rate constant plots of green synthesized AgNPs on KB-300 and KB-600 (b)

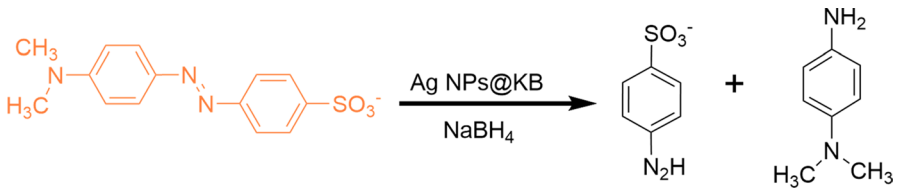


Fig. 8 Schematic illustration of MO degradation process in the presence of green synthesized AgNPs on KB-300 and KB-600

owing to the large surface area of KB-600. The rate constants corresponding to the green synthesized catalysts AgNPs@KB-300 and AgNPs@KB-600 along with KB-300 and KB-600 are shown in Fig. 7b. These were 0.0782, 0.0966, 0.320 and 0.622 min^{-1} , respectively. When the AgNPs@KB-300 and AgNPs@KB-600 nanocatalysts were added to MO solution, the color of the solution changed from orange to colorless within 10 and 6 min, respectively. The 464 nm and 272 nm peaks also almost disappeared, indicating the complete decomposition of the MO molecules. AgNPs@KB-300 and AgNPs@KB-600 exhibited ~99% MO degradations in 10 min and 6 min, respectively, owing to the high surface area of KB-600 and because the AgNPs well decorated. The rate constant corresponding to AgNPs@KB-600 was substantially higher than that corresponding to KB-300 and KB-600. This indicated the influence of the AgNPs on the surface of the Ketjen black.

A possible mechanism pathway of MO dye by the AgNPs@KB-600 nanocatalyst in the presence of NaBH_4 is illustrated in Fig. 8. In the suggested mechanism, carbon-based materials serve as a co-catalyst, prevent the aggregation. They also provide basic sites that promote the electron (e^-) transfer from the catalyst, which improves the catalytic activity [49]. The MO dye is electrophilic, whereas BH_4^- ions are nucleophilic and can adsorb on the surface of the catalyst. AgNPs@KB-600 accepts electrons from the BH_4^- and transfer it to the adsorbed MO molecules fastly [50]. The uptake e^- leads to the degradation of MO via an oxidation–reduction reaction [51, 52]. In this manner, the catalytic reduction process comprises e^- transfer from the BH_4^- to the adsorbed MO dye through the AgNPs@KB-600 nanocatalyst surface in aqueous media [50, 52–54].

Conclusion

In this study, plant-based AgNPs were decorated on KB-300 and KB-600 for catalytic methyl orange dye degradation. AgNPs@KB-300 and AgNPs@KB-600 showed an excellent catalytic dye degradation of approximately 99%. The reaction was completed within 6 min. Hence, we believe that the synthesized AgNPs@KB-300 and AgNPs@KB-600 could be used as green catalysts to treat wastewater generated from dyeing.

Acknowledgements This research was reinforced by the National Research Foundation of Korea (NRF) (2018R1A2B6006056 and 2020R1A2C1012439)

References

1. B. Lellis, C.Z. Fávoro-Polonio, J.A. Pamphile, J.C. Res. Innoavat. **3**, 275 (2019)
2. E. Bazrafshan, A.A. Zarei, H. Nadi, M.A. Zazouli, Ind. J. Chem. Technol. **21**, 105 (2014)
3. A. Mittal, A. Malviya, D. Kaur, J. Mittal, L. Kurup, J. Hazard. Mater. **148**, 229 (2007)
4. B. Lellis, C.Z.F. Polonio, J.A. Pamphile, J.C. Polonio, Biotechnol. Res. Innovation **3**, 275 (2019)
5. B. Vellaichamy, P. Periakaruppan, Silver nanoparticle-embedded RGO-nanosponge for superior catalytic activity towards 4-nitrophenol reduction. RSC Adv. **6**, 88837 (2016)
6. C.Q. Quiroz, N.A.J.Z. Giraldo, L.E. Botero, J. Quintero, D.Z. Triviño, J. Saldarriaga, V.Z. Pérez, Biomat. Res. **23**, 27 (2019)
7. S. Kondaiah, G. Bhagavanth Reddy, P. Babu, K. Kishore Kumar, G. Narasimha, J. Nanostr. Chem. **8**, 179 (2018)
8. Z. Zhao, N. Chamele, M. Kozicki, Y. Yao, C. Wang, J. Mater. Chem. C **7**, 6099 (2019)
9. M. Wang, C. Liu, H. Yang, J. Li, X. Ren, Poly. Comp. **35**, 1325 (2014)
10. M. Starowicz, B. Stypula, J. Banaś, Electrochem. Commu. **8**, 227 (2006)
11. S. Gurunathan, Arabian J. Chem. **12**, 168 (2019)
12. G. Krishna, V. Pranitha, M.A. Singara Charya, Open Nano **2**, 64 (2017)
13. P.C. Nagajyothis, L. Veeranjanya Reddy, K.C. Devarayapalli, S.V. Prabhakar Vattikuti, Y.J. Wee, J. Shim, J. Cluster Sci. (2020). <https://doi.org/10.1007/s10876-020-01821-8>
14. Y. He, F. Wei, Z. Ma, H. Zhang, Q. Yang, B. Yao, Z. Huang, J. Li, C. Zenga, Q. Zhang, RSC Adv. **7**, 39842 (2017)
15. P.C. Nagajyothis, M. Pandurangan, S.V.P. Vattikuti, C.O. Tettey, T.V.M. Sreekanth, J. Shim, Sep. Purif. Technol. **188**, 228 (2017)
16. P. Parvathi Ameena Jose, M.S. Kala Nandakumar Kalarikkal, S. Thomas, Res. Chem. Intermed. **44**, 5597 (2018)
17. T.V.M. Sreekanth, M.-J. Jung, I.-Y. Eom, Appl. Surf. Sci. **361**, 102 (2016)
18. S. Mohan, O.S. Oluwafemi, S.P. Songca, D. Rouxel, P. Miska, F.B. Lewu, N. Kalarikkal, S. Thomas, Pure Appl. Chem. **88**, 71 (2016)
19. C. Karuppiyah, K. Muthupandi, S.M. Chen, M. Ajmal Ali, S. Palanisamy, A. Rajan, P. Prakash, FahadMA Al-Hemaid, B.S. Lou, RSC Adv. **5**, 31139 (2015)
20. S. Gurunathan, J.W. Han, J.H. Park, E. Kim, Y.J. Choi, D.N. Kwon, J.H. Kim, Int. J. Nanomed. **10**, 6257 (2015)
21. T.V.M. Sreekanth, M. Pandurangan, Y.R. Min-Ji Jung, I.-Y. Lee, Res. Chem. Intermed. **45**, 5665 (2016)
22. P.O. Patil, P.V. Bhandari, P.K. Deshmukh, S.S. Mahale, A.G. Patel, S.B. Bari, Res. Chem. Intermed. **43**, 3757 (2017)
23. G. Cheng, G. Liu, P. Liu, L. Chen, S. Han, J. Han, F. Ye, W. Song, B. Lan, M. Sun, L. Yu, Front. Chem. **7**, 766 (2019)
24. Y. Liang, Y. Li, H. Wang, J. Zhou, J. Wang, T. Regier, H. Dai, Nat. Mater. **10**, 780 (2011)
25. Y. Tong, S. Bohm, M. Song, Austin J. Nanomed. Nanotech. **1**, 1003 (2014)
26. Y. Chen, X. Bai, Catalysts **10**, 142 (2020)
27. F. Alimohammadi, M.P. Gashti, A. Shamei, A. Kiumarsi, Superlatt. Microstru. **52**, 50 (2012)
28. R.S. Das, S.K. Warkhade, A. Kumar, A.V. Wankhade, Res. Chem. Intermed. **45**, 1689 (2019)
29. R. Cardena, B. Cercado, G. Buitrón, Biohydrogen, 159 (2019)
30. X. Qian, L. Jin, L. Zhu, S. Yao, D. Rao, X. Shen, X. Xi, K. Xiao, S. Qin, RSC Adv. **6**, 111190 (2016)
31. H. Dong, Y. Xu, M. Ji, H. Zhang, Z. Zhao, C. Zhao, Electrochim. Acta **151**, 118 (2015)
32. Y. Holade, C. Morais, K. Servat, T.W. Napporn, K. Boniface Kokoh, Phys. Chem. Chem. Phys. **16**, 25609 (2014)
33. J. Chen, N. Zhou, H. Wang, Z. Peng, H. Li, Y. Tang, K. Liu, Chem. Commun. **51**, 10123 (2015)
34. D. Wang, J. Wang, X. Luo, Z. Wu, L. Ye, ACS Sustain. Chem. Eng. **6**, 983 (2018)
35. Y. Zhou, B. Wang, C. Liu, N. Han, X. Xu, F. Zhao, J. Fan, Y. Li, Nano Energy **15**, 654 (2015)
36. Y. Hamauzu, C. Kume, H. Yasui, T. Fujita, J. Agri. Food Chem. **55**, 1221 (2007)
37. E.K. Essuman, P.C. Nagajyothis, C.O. Tettey, J. Med. Plants Stud. **5**, 175 (2017)
38. P.C. Nagajyothis, T.V.M. Sreekanth, K.D. Lee, Synth. React. Inorg. Metal-Org., Nano-Metal Chem. **42**, 1339 (2012)

39. S. Chen, G. Yang, S. Luo, S. Yin, J. Jia, Z. Li, S. Gao, Y. Shao, K. Yao, *J. Mater. Chem A* **5**, 14230 (2017)
40. S. Xie, Y. Xie, J.J. Kruzic, K. Gu, H. Yang, Y. Deng, X. Zeng, *Chem. Cat. Chem.* **12**, 750 (2020)
41. C.D. Zappiello, D.M. Nanicuacua, W.N.L. dos Santos, D.L.F. da Silva, L.H. Dall'Aantônia, F.M. de Oliveira, D.N. Clausen, C.R.T. Tarley, *J. Braz. Chem. Soc.* **27**, 1715 (2016)
42. Md Amdadul Huq, *Int. J. Mol. Sci.* **21**, 1510 (2020)
43. K. Jyothi, M. Baunthiyal, A. Singh, *J. Rad. Res. Appl. Sci.* **9**, 217 (2016)
44. P. Devaraj, P. Kumari, C. Aarti, A. Renganathan, *J. Nanotechnol.* **2013**, 598328 (2013)
45. Y. Xu, J. Chen, Z. Xiao, C. Ou, W. Lv, L. Tao, S. Zhong, *Nanoscale* **11**, 15881 (2019)
46. J. Li, L. Kang, B. Wang, K. Chen, X. Tian, Z. Ge, J. Zeng, J. Xu, W. Gao, *ACS Sustain. Chem. Eng.* **7**, 1146 (2019)
47. M. Hou, F. Li, X. Liu, X. Wang, H. Wan, *J. Hazard. Mat.* **145**, 305 (2007)
48. G.R. Dillip, T.V.M. Sreekanth, S.W. Joo, *Ceram. Inter.* **43**, 6437 (2017)
49. F. Xiao, H. Ren, H. Zhou, H. Wang, N. Wang, D. Pan, *ACS Appl. Nano Mater.* **2**, 5420 (2019)
50. A. Ucar, M. Findik, I.H. Gubbuk, N. Kocak, H. Bingol, *Mat. Chem. Phys.* **196**, 21 (2017)
51. S. Li, H. Li, J. Liu, H. Zhang, Y. Yang, Z. Yang, L. Wang, B. Wang, *Dalton Trans.* **44**, 9193 (2015)
52. G. Fu, L. Tao, M. Zhang, Y. Chen, Y. Tang, J. Lin, T. Lu, *Nanoscale* **5**, 8007 (2013)
53. P.K. Sahoo, D. Thakur, D. Bahadur, B. Panigrahy, *RSC Adv.* **6**, 106723 (2016)
54. B. Vellaichamy, P. Periakaruppan, *RSC Adv.* **6**, 31653 (2016)

Publisher's Note Springer Nature remains neutral with regard to jurisdictional claims in published maps and institutional affiliations.